EES Catalysis

Accepted Manuscript

This article can be cited before page numbers have been issued, to do this please use: A. Chhetri, A. Karmakar, H. Girase, S. Tothadi, S. Maniam, K. Wilson, A. F. Lee, S. Kundu and J. Mitra, *EES Catal.*, 2026, DOI: 10.1039/D6EY00112B.

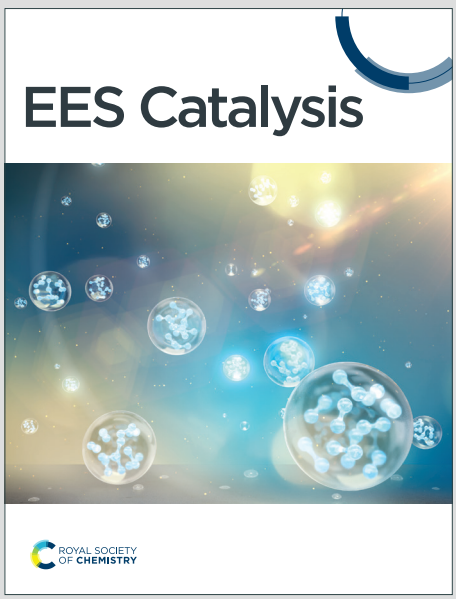

Broader context statement

DOI: 10.1039/D5EY00112B

Water splitting is the only route to so-called 'green hydrogen' wherein the hydrogen evolution reaction (HER) and oxygen evolution reaction (OER) are driven by light or renewable electricity. Green hydrogen is an important energy vector, zero emission fuel, and critical feedstock for sustainable chemical manufacturing, and requires photo- and electrocatalytic technologies deployable at global scale. The former is currently inefficient, and the latter typically requires scarce/expensive metals and complex inorganic syntheses with a significant environmental impact. In this study, we report the low-cost and scalable synthesis of metal-free electrocatalysts based on melamine and tartaric acid that are active and stable for water splitting in corrosive environments. Tartaric acid can exist in chiral or racemic forms within the organocatalysts that undergo different interactions with the electrons responsible for water splitting. Chiral organoelectrocatalysts selectively promote HER and OER by increasing the number/accessibility of active sites, and potentially inducing spin-polarisation of radicals at the catalyst surface. These results highlight the promise of organoelectrocatalysts for supporting a sustainable hydrogen economy and mitigating the broader environmental footprint of electrochemical processes.

Chirality-enhanced oxygen and hydrogen production by water splitting over a hydrogen-bonded organoelectrocatalyst

View Article Online
DOI: 10.1039/D6EY00112B

Ashis Chhetri,[a,b,c] Arun Karmakar,[b,d] Harpal Gorakh Girase,[a,b,h] Srinu Tothadi,[b,e] Subashani Maniam,[c] Karen Wilson,[f] Adam F. Lee,[g*] Subrata Kundu,[b,d*] and Joyee Mitra[a,b,h*]*

[a]Inorganic Materials & Catalysis Division, CSIR-Central Salt & Marine Chemicals Research Institute, Bhavnagar 364002, Gujarat, India
[b]Academy of Scientific and Innovative Research (AcSIR), Ghaziabad 201002, India
[c]School of Science, STEM College, RMIT University, Melbourne, VIC 3000, Australia
[d]Electrochemical Process Engineering Division, CSIR-Central Electrochemical Research Institute, Tamil Nadu, India
[e]Marine Elements and Marine Environment Division and Centralized Instrument Facility, CSIR-Central Salt & Marine Chemicals Research Institute, Bhavnagar 364002, Gujarat, India
[f]Centre for Catalysis & Clean Energy, Griffith University, Gold Coast Campus, QLD 4222, Australia
[g]Institute of Materials Research and Engineering, Agency for Science Technology and Research, Singapore 138632, Singapore.
[h] *Materials Chemistry & Interfacial Engineering, CSIR-Institute of Minerals & Materials Technology, Bhubaneshwar 751013, Odisha, India.*

Corresponding authors: Chhetri.Ashis@nims.go.jp; skundu@cecri.res.in; Adam_Lee_from.tp@a-star.edu.sg; joyeemitra@csmcri.res.in

Abstract

Electrocatalytic water splitting has emerged as the most promising source of renewable hydrogen to support energy conversion/storage and chemical manufacturing as a part of the global circular economy. However, overall water splitting to produce green H_2 through the hydrogen evolution reaction (HER) is limited by the high overpotential and sluggish kinetics of the associated oxygen evolution reaction (OER). Control over electron spin at the electrode-electrolyte interface may lower the thermodynamic barriers, and hence improve the catalytic efficiency, of both reactions. We employ compositionally identical chiral and racemic hydrogen-bonded organocatalysts, comprised of (ionised) melamine and L-, D-, or DL-tartaric acid, to demonstrate chirality-enhanced organoelectrocatalysis. Chiral electrocatalysts promote both OER and HER compared to their racemic counterpart, as evidenced by lower overpotential (384 (L)/379 (D) mV vs 483 mV (DL) for OER, and 143 mV (L)/144 mV (D) vs 358 mV (DL) for HER), a change in the rate-determining step, and an approximately four-fold increase in current density. This work highlights the impact of catalyst chirality on enhancing electrocatalytic water splitting to hydrogen and oxygen, and the promising performance of inexpensive and environmentally benign organoelectrocatalysts.

Keywords: Organocatalysis; Water splitting; spin control; oxygen evolution reaction; hydrogen evolution reaction

1. Introduction

An ever-rising demand for (renewable) energy and remediation of environmental problems arising from anthropogenic CO_2 emissions is promoting a transition away from fossil fuels to a sustainable hydrogen economy.[1, 2] Renewable energy technologies, notably photo- and electrocatalytic water splitting, are the most effective ways to produce 'green' hydrogen as an energy vector, fuel and chemical feedstock for the chemical industry.[3-5] In addition to the hydrogen evolution reaction (HER), water splitting necessitates the parallel oxygen evolution reaction (OER). The latter proceeds through multiple, proton-coupled electron transfer steps that exhibit slow kinetics and generate numerous radicals (including *OH, *O and *OOH) and hence low selectivity, representing a bottleneck to H_2 from water electrolysis. The high overpotential for electrocatalytic OER typically accounts for most of the energy input in overall water splitting,[5, 6] with the co-production of undesired and problematic H_2O_2.[7, 8] The complexity of OER has focused research efforts on identifying catalysts that permit more favourable energetics. Catalyst activity often depends on the relative binding energies of reactive intermediates at the catalyst surface, governed under equilibrium conditions by the Sabatier principle.[9] Water electrolysis is typically run under harsh acidic or alkaline conditions, which necessitate the use of scarce and expensive catalysts based on Pt (for HER)[10] and Ir, Ru (for OER) [11] for high activity and stability. The low abundance of these elements in the Earth's crust suggests their total depletion in the next 20-50 years at current usage unless new associated mineral deposits are discovered.[12] However, even if such deposits are found, their associated geopolitical issues may hinder widespread access and hence decarbonisation of the global energy sector to achieve UN sustainable development goals.[13] Hence there is an urgent need for Earth-abundant alternatives to Platinum Group metals listed in the EU 2023 critical raw material list.[14] Although strategies to alter the binding energies of water and reactive intermediates have improved the catalyst design, alternative approaches such as the effect of magnetic fields and electronic spin on reaction kinetics are less explored.[15-18]

Electrocatalysis is characterised by electron transfer at the electrode-electrolyte interface. Electron transfer through a chiral molecule can reportedly induce spin polarisation, without application of an external magnetic field, wherein the chiral molecule acts as a spin filter to create an imbalance between 'up' and 'down' electron spins.[19-24] This phenomenon, termed chiral-induced spin selectivity (CISS),[25] was reported to occur at electrode-electrolyte interfaces, and to promote OER wherein spin constraints dictate the possible radical intermediates formed, favouring the triplet ground state of dioxygen.[17, 26] Waldeck, Naaman and other researchers have utilised CISS to lower the overpotential required for OER. and to avoid singlet H_2O_2 by-product formation, without using a magnetic field.[25,27-34] However, these studies are limited to intrinsically chiral metal oxides or metal oxide surfaces functionalised by chiral adsorbates. These systems suffer from poor adsorption of the chiral modifier and electrode, decreasing operational lifetime; lower current densities for such functionalised versus bare electrocatalysts, e.g., due to site-blocking of the electrocatalytic active sites on the metal oxide; and in situ corrosion of metal-oxide electrodes.[29, 35] Organoelectrocatalysts, including heteroatom-doped carbon materials,[36, 37] covalent organic frameworks,[38-40] and charge-assisted systems,[42-44] have also been studied for OER, but to our knowledge, differences between racemic and chiral analogues have never been demonstrated in organoelectrocatalysts for water splitting, despite the many benefits of organic systems compared to metal-containing counterparts.[44] Although there are literature reports that chirality (through CISS) can improve OER, there is only one report of its impact on HER for photoelectrochemical H_2 production over conductive, polymer electrodes.[45]

Herein, we highlight the benefits of hydrogen-bonded organocatalysts containing a chiral constituent for electrocatalytic water splitting, namely lower overpotentials, higher current densities, and faster electron transfer across the electrode-electrolyte interface for both OER and HER. Charge-assisted, hydrogen-bonded, chiral organoelectrocatalysts were prepared from melamine and either L-(+)-tartaric acid (**MeLTA-C**) or D-(-)-tartaric acid (**MeDTA-C**), with identical compositions to a racemic counterpart prepared from melamine and DL-tartaric acid (**MeTA-rac**). Chiral **MeLTA-C** and **MeDTA-C** displayed superior catalytic activity than **MeTA-rac** for both OER and HER, evidenced by a lower overpotential (OER: 384 mV (L)/ 379 mV (D) versus 483 mV (DL); HER: 143 mV (L)/144 mV (D) versus 358 mV (DL)) at 10 $mA.cm^{-2}$. **MeLTA-C/MeDTA-C** also displays a significantly lower interfacial electron transfer resistance and corresponding four-fold enhancement in OER and HER versus **MeTA-rac**.

2. Materials and Methods

2.1 Catalyst Synthesis

In a typical synthesis of **MeLTA-C**, melamine (2 mmol, 252 mg) and L-(+)-tartaric acid (L-TA, 1 mmol, 150 mg) were combined and thoroughly ground in an agate mortar and pestle to obtain a homogeneous mixture. The resulting solid was transferred to a Teflon-lined stainless-steel autoclave, followed by the addition of 30 mL of Milli-Q water. The sealed autoclave was heated in a hot-air oven to 120 °C at a controlled heating rate of 2 °C min^{-1} and maintained at this temperature for 60 h. The reaction time was recorded once the target temperature was reached. After completion, the autoclave was allowed to cool naturally to room temperature. The resulting white crystalline solid was collected by gravity filtration using Whatman filter paper and thoroughly washed with lukewarm water to remove any unreacted melamine and residual L-TA. The product was then dried under ambient conditions to yield the hydrogen-bonded organic system **MeLTA-C**. **MeDTA-C** and **MeTA-rac** were synthesized under the same conditions using D-(–)-tartaric acid and racemic tartaric acid, respectively. The isolated yields of all hydrogen-bonded systems were >90 %, even for a 960 mg scale-up (**Table S1**). However, attempts to synthesize an analogous melamine–meso-tartaric acid system under identical conditions did not result in diffraction quality crystals. All the hydrogen bonded systems are successfully characterized using different analytical techniques such as XRD, FTIR, CP-MAS NMR, XPS etc. (Details in SI and in Result and Discussions Section).

2.2 Electrocatalysis

All electrochemical measurements were performed using a Metrohm Autolab M204 electrochemical analyzer. Hg/HgO (1 M KOH) or Hg/Hg_2SO_4 reference electrodes (CH Instruments) were employed for measurements in alkaline and acidic electrolytes, respectively, while a graphite rod (Alfa Aesar) served as the counter electrode. Potentials were initially recorded versus the Hg/HgO or Hg/Hg_2SO_4 reference electrodes and subsequently converted to the reversible hydrogen electrode (RHE) scale using the appropriate modified Nernst equations (Full details in the Result and Discussion section and in SI).

3. Results and Discussions

3.1. Catalyst Synthesis and Characterization

Hydrothermal reaction of melamine with L-(+)-tartaric acid, D-(-)-tartaric acid or DL-tartaric acid (a 1:1 molar ratio of the enantiomers) at 120 °C yielded colourless crystals designated **MeLTA-C**, **MeDTA-C**, and **MeTA-rac**, respectively (**Figure 1a**). Temperature strongly influences such reactions as the pK_a falls with increasing temperature, facilitating

protonation of the melamine ring under hydrothermal conditions.[46] Lower temperatures precluded proton transfer from tartaric acid to melamine, while temperatures >120 °C induced their decomposition. Single crystal X-ray diffraction evidenced **MeLTA-C, MeDTA-C** and **MeTA-rac** formed monoclinic crystals: **MeLTA-C/MeDTA-C** in the chiral space group *C2*; and **MeTA-rac** in the achiral *C2/c* space group (**Table S2**). We were unable to grow diffraction quality crystals of melamine with meso-tartaric acid under identical conditions. Unit cells of all crystalline materials contained a completely deprotonated tartrate anion and two (singly protonated) melaminium cations, providing charge balancing, in addition to molecular water (**Figure 1b-d**). Crystal structures of **MeLTA-C** and **MeDTA-C** contain two H_2O molecules and 0.25 H_2O in the asymmetric unit, the O atom of the third water molecule occupies a special position (two-fold axis with an occupancy of 0.25) with the associated two H atoms in general positions (with 0.25 occupancies).

Two crystallographically independent melaminium moieties participated in charge-assisted hydrogen bonding with the tartrate dianion as a proton acceptor, assisted by lattice water molecules. Water molecules acted as bifurcated H-bond donors, interacting with different -NH_2 and -NH^+ centres via N-H···O H-bonding interactions (N···O distances ranging from 2.81-3.10 Å) (**Figure 1e-g**).[47] Each tartrate molecule interacted with the -OH group of another tartrate unit via O-H···O H-bonding (average distance ~2.71 Å) and with lattice water molecules at an O-O distance of ~2.69 Å. The -NH_2 and -NH^+ centres of the cationic melaminium N-H participated in H-bonding with CO_2^- and -OH groups of tartrate anions with a distance of ~2.80-2.96 Å, while the adjacent melaminium units interact via N-H···N hydrogen bonding (average N-N distance 3.03 Å). Additionally, an average distance of ~3.44 Å between two melaminium planes indicated strong π-π stacking interactions (**Figure S1**).[48] Overall, the cationic and anionic counterparts interact through extensive intermolecular hydrogen bonding interactions among themselves, assisted by lattice water molecules (**Figure 1e-g**). Thus, the hydrogen bonded chiral and racemic systems are stabilised by long-range hydrogen-bonded networks consisting of cationic and anionic moieties, interconnected by lattice water molecules, thereby enhancing the stability of the overall system via multiple hydrogen-bonded interactions. Hydrogen bonding in **MeLTA-C**, **MeDTA-C** and **MeTA-rac** was confirmed by powder XRD at 100 °C, wherein peak broadening and shifting were observed due to dehydration and a resultant loss of material crystallinity (**Figures S4-S5**). **MeLTA-C**, **MeDTA-C**, and **MeTA-rac** exhibit similar FTIR spectra due to their common chemical functional groups (**Figure S2**). The hydroxyl stretch at 3362 cm^{-1} is attributed to molecular water and O-H groups in tartrate anions. A broad signal associated with N-H stretches of the exocyclic groups in melaminium cation was observed ~3072 cm^{-1}. A slight blue shift in the latter for **MeLTA-C**. **MeDTA-C**, and **MeTA-rac** compared to pure melamine is ascribed to the participation of exocyclic -NH_2 groups in hydrogen bonding networks. A sharp band at 1689 cm^{-1} was observed due to the C=O group in the tartrate anion.[49] Triazine C=N vibrations induced a band at ~1596 cm^{-1}, with ring breathing and deformation (out-of-plane bends) at 985 cm^{-1} and 772 cm^{-1} respectively (**Figure S2**).[50]

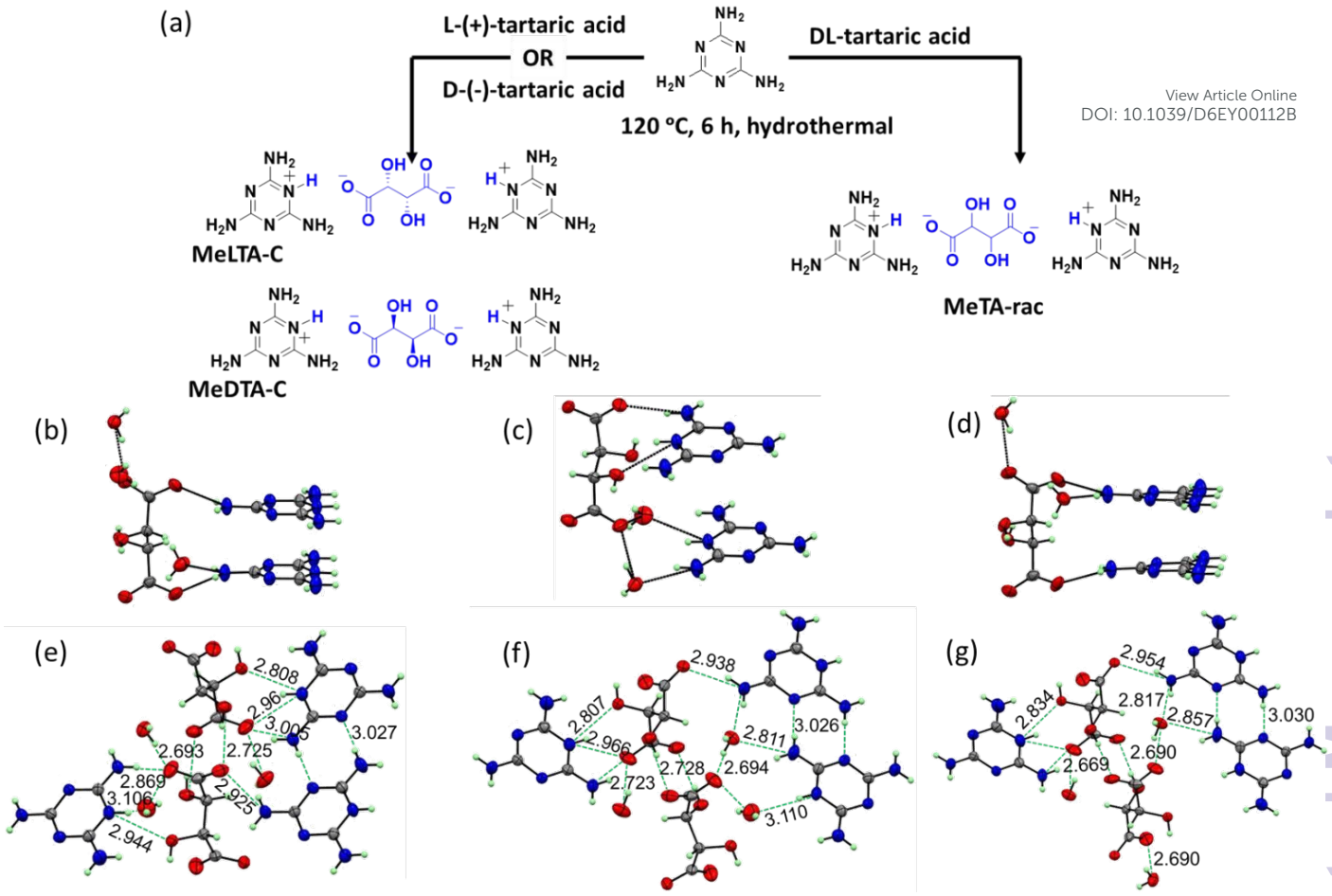

Figure 1. (a) Schematic of the hydrothermal synthesis of **MeLTA-C**, **MeDTA-C**, and **MeTA-rac**; crystal structures of (b) **MeLTa-C**, (c) **MeDTA-C**, and (d) **MeTA-rac**, respectively (50 % probability thermal ellipsoid level); hydrogen-bonding networks in (e) **MeLTa-C**, (f) **MeDTA-C**, and (g) **MeTA-rac**, respectively. Donor-acceptor distances in Å.

^{13}C CP-MAS NMR spectrum of **MeLTA-C** showed four distinct carbon species. Carbon atoms in the protonated melaminium rings appear as singlet peaks at 168.26 and 160.63 ppm, whereas those associated with the carboxylate and hydroxyl groups of tartrate anions appear as doublets at ~185.90 ppm, and ~80.0 ppm, respectively (**Figure 2a**). The corresponding ^{15}N CP-MAS NMR spectrum of **MeLTA-C** exhibited three peaks arising from the three different types of nitrogen atoms, i.e. protonated ring nitrogens at -279.20 ppm, unprotonated ring nitrogens at ~ -263.23 ppm, and exocyclic amines at -291.51 ppm (**Figure 2b**).[51] Peak integration confirmed the number of each nitrogen and was consistent with melamine.

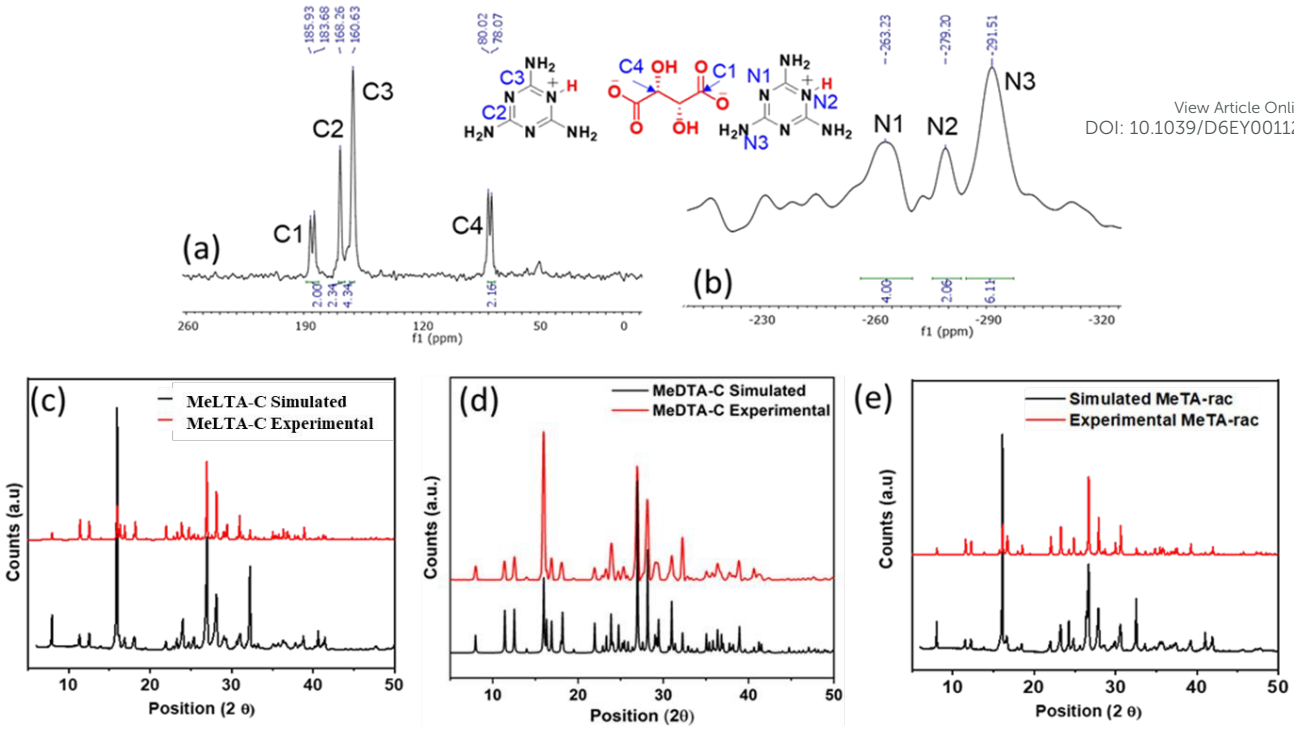

Figure 2. (a) ^{13}C and (b) ^{15}N CP-MAS NMR of **MeLTA-C**, and experimental and simulated powder XRD diffractograms of (c) **MeLTA-C**, (d) **MeDTA-C** and (e) **MeTA-rac**, respectively. The simulated patterns were obtained from their respective single crystal structures.

Powder XRD diffractograms of **MeLTA-C**, **MeDTA-C**, and **MeTA-rac** confirmed their high crystallinity (**Figure 2c-e**), with major reflections at 2θ ≈7.2° and ≈27.2° characteristic of deformed triazine rings and stacked triazine rings, respectively.[52] These diffractograms were distinctive from those of the tartaric acid and melamine precursors, but a good match to powder patterns simulated from their single crystal structures, evidencing high phase purities (**Figure 2c-e** and **Figure S3**). Note there was no evidence of metal impurities by bulk or surface elemental analysis (ICP or XPS).

Surface chemical environments of **MeLTA-C**, **MeDTA-C**, and **MeTA-rac** were analysed by XPS, with corresponding survey spectra confirming the presence of C, N, and O in similar compositions in all three cases (**Figure S6a-c** and **Table S3**). High-resolution C 1s XP spectra of the chiral **MeLTA-C** and **MeDTA-C** were fitted to four components, indicative of C-C (284.8 eV) for adventitious carbon, C-OH (286.3 eV), COO^- (288.9 eV) of tartrate, and $C{=}N_3$ for the triazine ring (288.4 eV) carbons in melamine (**Figure 3a,d**). A weak peak at ~286 eV was also required for the fit, indicative of the presence of $C\text{-}NH_2$ (4 atom% of total surface carbon) likely formed from a small fraction of degraded melamine. The 1:1:3 ratio of $COH:COO^-:C{=}N_3$ components is in good agreement with the integrated ^{13}C CP-MAS-NMR in **Figure 2a**. **MeTA-rac** was fitted with the same C 1s components in a similar intensity ratio (**Figure 3g**). Corresponding N 1s spectra of all the organic materials exhibited two distinct chemical environments associated with three exocyclic $\text{-}NH_x$ (399.2 eV) and three ring $C{=}N_3$ (400.13 eV) in melaminium (**Figure 3b,e,h**), along with a π-π* satellite at 406.4 eV from the aromatic ring. The N 1s components for NH_x and $C{=}N_3$ are in a 2:1 ratio.[53] Three distinct O 1s environments were also observed for **MeLTA-C**, **MeDTA-C**, and **MeTA-rac**, associated with COO^- (531.2 eV) and C-OH (532.5 eV) species in tartrate anions (**Figure S6d-f**) and terminal COO^- species at 534.2 eV likely hydrogen bonded to ring N of melamine. As expected for enantiomers, the ratios of each type of surface carbon, nitrogen and oxygen species were very similar between **MeLTA-C, MeDTA-C**, and **MeTA-rac**. Microstructural analysis of

MeLTA-C, **MeDTA-C**, and **MeTA-rac** by FE-SEM revealed rectangular plates in all cases (**Figure 3c,f,i**), although there were some differences in their packing arrangement: rectangular plates in **MeLTA-C** and **MeDTA-C** radiate outward from a common centre and are arranged in a spiral manner consistent with a specific 'handedness', whereas the plates in **MeTA-rac** were randomly arranged. Energy dispersive X-ray (EDX) analysis and elemental mapping confirmed carbon, nitrogen, and oxygen were uniformly distributed throughout both materials, in similar atomic ratios (**Figure S7-S9** and **Table S4**).

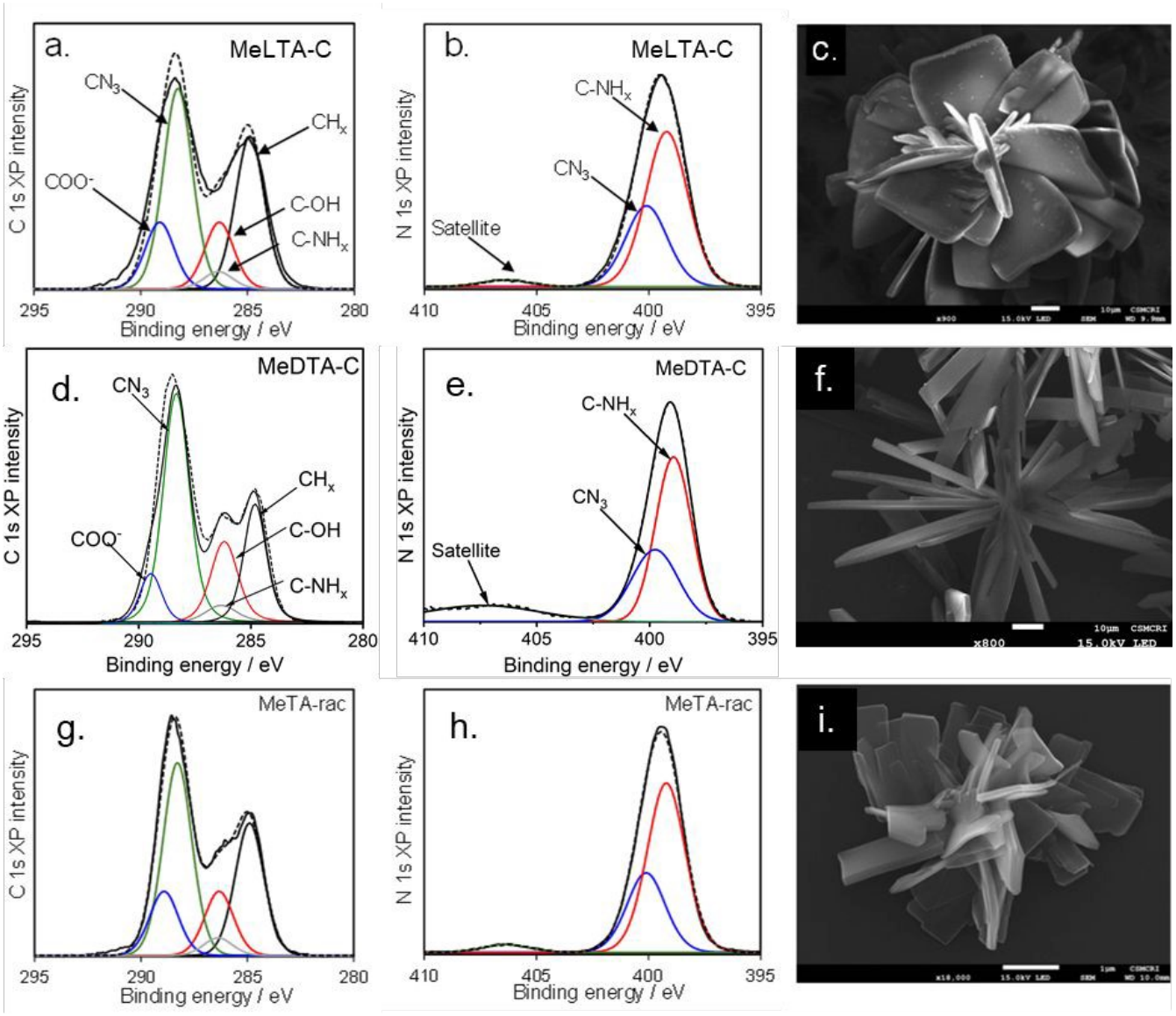

Figure 3. Fitted C 1s and N 1s XP spectra of (a-b) **MeLTA-C**, (d-e) **MeDTA-C**, and (g-h) **MeTA-rac**, and corresponding FESEM micrographs of (c) **MeLTA-C**, (f) **MeDTA-C**, and (i) **MeTA-rac**.

The chiroptical properties of **MeLTA-C/MeDTA-C** and **MeTA-rac** were examined by measuring their optical rotation (α) as aqueous suspensions; plane polarised light was rotated clockwise by +0.029° whereas anticlockwise by -0.028° on passing through **MeLTA-C** and **MeDTA-C** respectively, confirming their chiral nature,[54] but was unaffected by **MeTA-rac** (**Table S5**). Although free D/L-tartaric acids exhibited rotations of ±12.24°, optical activity is often lowered by hydrogen bonding due to conformational constraints imposed. Haghdani et al reported a similar magnitude optical rotation in (S)-1-(2-naphthyl)-1-fluoroethanol, (R)-1,1,1-trifluoro-2-phenylethanol, and (R)-1-(4-phenoxyphenyl)-2-fluoroethanamine.[55] Thermogravimetric analysis revealed similar behaviour for **MeLTA-C** and **MeTA-rac** under air (**Figure S10**), with an initial mass loss at ~150 °C attributed to the desorption of H-bonded lattice water, indicating

excellent thermal stability for many practical applications.[56] Decomposition of both dehydrated materials occurred in two principal stages, >280 °C and > 500 °C, with **MeLTA-C** exhibiting slightly greater stability. The chemical stability of **MeLTA-C** and **MeTA-rac** was also explored by their 12 h immersion in 1 M acid and alkaline solutions; powder XRD and FE-SEM evidenced negligible change in the crystallinity or morphologies of both materials (**Figure S11**) and hence high chemical stability across a wide pH range.

3.2. Electrocatalytic water splitting

Oxygen evolution reaction (OER)

The electrophilic carbon centre adjacent the protonated nitrogen in the triazine ring of **MeLTA-C, MeDTA-C** and **MeTA-rac** can react with adsorbed hydroxyl intermediates (*OH) formed during OER, and is considered the corresponding active sites for OER.[44] Conversely, nitrogen atoms in a triazine ring are readily protonated, and are considered the active sites for HER.[57] Chiral materials and molecules are reported to induce spin polarisation of electrons with (or without) a net charge flow, the so-called CISS effect that connects chiral symmetry and electron spin.[16, 19] Photoelectrochemical H_2 production from water is reported to benefit from the CISS effect.[45] We therefore hypothesised that **MeLTA-C** and **MeDTA-C** might exhibit spin-filtering of electrons through CISS under an applied potential, favouring the formation of triplet $^3\Sigma$ (versus singlet $^1\Delta$) O_2 and suppressing H_2O_2 formation (**Figure 4a**).

MeLTA-C, **MeDTA-C** and **MeTA-rac** were prepared as catalyst inks using a Nafion binder, and drop-cast on a carbon cloth working electrode as per literature methods.[58] Linear sweep voltammograms (LSV) were recorded with a slow scan rate of 5 $mV.sec^{-1}$ in a N_2-saturated 1 M KOH electrolyte (**Figure 4b**). The overpotential to achieve a current density of 10 $mA.cm^{-2}$ was much lower for the **MeLTA-C** (and **MeDTA-C**) organocatalysts than the compositionally identical **MeTA-rac**, being 384 mV (379 mV) versus 483 mV respectively. **MeLTA-C** also exhibited lower overpotentials than **MeTA-rac** at higher current densities (15 $mA.cm^{-2}$ and 30 $mA.cm^{-2}$, **Figure S12a**), consistent with superior OER activity. Note that a reference IrO_2 catalyst required 453 mV overpotential to achieve the same current density under identical conditions (**Figure 4b**), and the overpotential for **MeLTA-C** is comparable to other organoelectrocatalysts (**Table S6**).[59, 60] At 1.68 V potential versus a reversible hydrogen electrode (RHE), **MeLTA-C** (and **MeDTA-C**) exhibited a four-fold increase in current density relative to **MeTA-rac** (**Figure 4b**). A possible explanation is that the chiral tartrate moiety in **MeLTA-C** promotes OER by spin filtering and the resulting selective formation of $^3\Sigma$ O_2 molecules via a low energy pathway, akin to the CISS effect reported for chiral molecules on metal oxides.[17, 30, 31] Note that competitive pathways to H_2O_2 are forbidden on a spin-polarised surface.[16, 30] Conservation of spin angular momentum during electron transfer between catalyst and reactants may further lower the activation barrier to OER.[19]

View Article Online
DOI: 10.1039/D6EY00112B

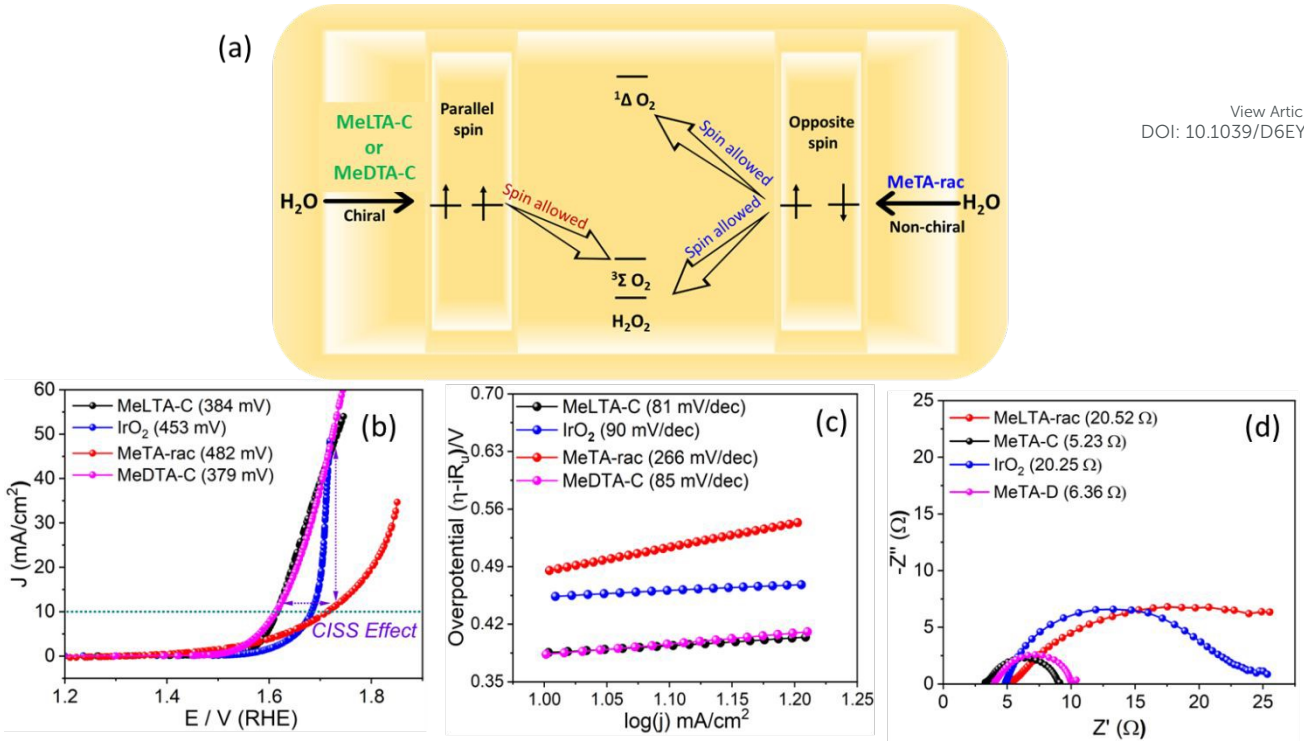

Figure 4. (a) Schematic of CISS effect in **MeLTA-C/ MeDTA-C** versus **MeTA-rac** for OER. (b) LSV plots of **MeLTA-C, MeDTA-C**, and **MeTA-rac** alongside an IrO_2 reference for OER in 1 M KOH under nitrogen, and corresponding (c) Tafel and (d) Nyquist plots, providing insight on OER kinetics and electron transfer dynamics at the electrode-electrolyte interface, respectively.

Reaction dynamics, evaluated from Tafel plots of iR drop-corrected LSV data, also indicated faster interfacial charge transfer for **MeLTA-C** and **MeDTA-C** than **MeTA-rac** (**Figure 4c**),[61] with a Tafel slope 81 mV.dec^{-1} for **MeLTA-C** and 85 mV.dec^{-1} for **MeDTA-C**, respectively, in accordance with a deprotonation rate-limiting step. Corresponding Tafel slopes for **MeTA-rac** and IrO_2 were 266 and 90 mV.dec^{-1}, respectively. The high Tafel slope for **MeTA-rac** indicates a different rate-determining step.[62] Computational studies indicate that transition state energies associated with multi-electron OER are influenced by spin alignment at the catalyst surface.[63] For **MeLTA-C** (and **MeDTA-C**), spin filtering would favour high spin multiplicity reaction intermediates to $^3\Sigma$ O_2, whereas **MeTA-rac** is expected to favour spin-paired intermediates that would necessitate an energy-intensive (possibly rate-determining) spin inversion to form the $^3\Sigma$ O_2 product.[64] Charge transfer resistance (R_{ct}) across the electrode-electrolyte interface was probed by electron impedance spectroscopy (EIS) at 1.6 V vs RHE (**Figure 4c**). The lower R_{ct} for **MeLTA-C** (5.2 Ω) and **MeDTA-C** (6.36 Ω) compared to **MeTA-rac** (20.5 Ω) and IrO_2 (20.3 Ω) is consistent with faster charge and mass transport over the chiral organocatalyst, ascribed to a spin channel for **MeLTA-C** and **MeDTA-C**, that facilitates electron transfer between adsorbed intermediates and active sites. Charge transport mediated by the spin-correlated chiral tartrate and *OH may impart a single spin state to all electrons; such parallel spin alignment being a prerequisite to form $^3\Sigma$ O_2. **MeLTA-C** evidenced excellent catalytic stability in 12 h chronoamperometry (CA) test at a constant potential of 1.68 V vs RHE (iR-uncorrected), with minimal decrease in current density (**Figure S12b**). Potentiodynamic stability of **MeLTA-C** was also evaluated through accelerated degradation (AD) experiments over 500 cycles at a scan rate of 100 mV.sec^{-1}, with a modest increase in overpotential (from 384 to 423 mV) observed after electrocatalysis in these alkaline conditions (**Figure S13a**). This small increase may reflect limited deprotonation of (protonated) melaminium rings during continuous cycling that might in turn adversely affect the electron deficiency of adjacent carbon centres in **MeLTA-C**.

A slight decrease in the OER activity of **MeLTA-C** after 500 cycles also manifest as a small increase in R_{ct} (to 8.65 Ω) across the electrode-electrolyte interface (**Figure S13b**). **MeLTA-C** was thus resistant to major surface reconstructions sometimes observed under alkaline OER.[65] The absence of evolved CO_2, often observed during decomposition of organoelectrocatalysts,[43] confirmed the chemical stability of **MeLTA-C**. Overall, **MeLTA-C** exhibited a Faradaic efficiency of ~90 % for O_2 evolution (**Figure S15**) and a corresponding turnover frequency (TOF, **Eq. S8**) of 6.1 sec^{-1}, indicative of an efficient OER organoelectrocatalyst. The electrochemically active surface area (ECSA), determined by the double layer capacitance (C_{dl}) method, revealed a higher calculated C_{dl} value for **MeLTA-C** than **MeTA-rac** of 22.44 and 11.47 $mF.cm^{-2}$, respectively, suggesting the chiral catalysts possessed twice the number of active sites for oxygen evolution (**Figure S14**). Although we cannot discount the occurrence of CISS in **MeLTA-C** (and **MeDTA-C**), this finding suggests a more prosaic explanation for the chiral performance enhancement; more active sites.

Hydrogen evolution reaction (HER)

The negative ζ-potential of **MeLTA-C** and **MeTA-rac** (**Figure S16** and **Table S7**) indicate that they present negatively charged tartrate anions at their crystal surfaces. We postulated that the negative surface potentials and high nitrogen content of the melaminium ring might aid proton adsorption and the consequent production of reaction intermediates for HER.[64] Electrocatalytic HER was therefore explored using a three-electrode assembly by drop-casting inks of **MeLTA-C, MeDTA-C** or **MeTA-rac** on carbon cloth. Linear sweep voltammograms (LSV) were recorded with a slow scan rate of 5 $mV.sec^{-1}$ in a N_2-saturated 0.5 M H_2SO_4 electrolyte (**Figure 5a**). As for OER, the reaction overpotential to achieve a current density of 10 $mA.cm^{-2}$ for HER was much lower for both **MeLTA-C** (143 mV) and **MeDTA-C** (144 mV) than the compositionally identical **MeTA-rac** (358 mV), albeit significantly higher than that of a reference Pt/C (18 mV). Consequently, at a fixed potential of -0.3 V RHE, the current density for **MeLTA-C** was ~8x greater than for **MeTA-rac**, and should be mirrored by a similar enhancement in evolved hydrogen productivity;[45] the lower onset potential for HER and rapid increase in cathodic current with more negative potential over **MeLTA-C** are attributed to rapid proton reduction. A lower overpotential for **MeLTA-C** versus **MeTA-rac** was also observed at higher current densities (20 $mA.cm^{-2}$ and 30 $mA.cm^{-2}$, **Figure S17**). The overpotentials for **MeLTA-C**/ **MeDTA-C** is lower than organoelectrocatalysts (including covalent triazine frameworks, **Table S8**).[66, 67]

Reaction dynamics, again evaluated from Tafel plots of iR drop-corrected LSV data (**Figure 5b**), evidenced fast interfacial charge transfer for the Pt/C electrocatalyst (29 $mV.dec^{-1}$) with the Heyrovsky step rate-limiting, i.e. the reaction of adsorbed hydrogen atoms at high surface coverage with a hydronium cation and electron. Heyrovsky- and Volmer-limited (discharge of a hydronium ion to form adsorbed hydrogen at low surface coverage and water) reactions are both reported under acidic conditions for Tafel slopes up to 120 $mV.dec^{-1}$, and hence HER over **MeLTA-C** (94 $mV.dec^{-1}$) and **MeDTA-C** (99 mV dec^{-1}) are likely also Heyrovsky/Volmer rate-limited. **MeTA-rac** exhibited slower charge transfer (Tafel slope of 195 $mV.dec^{-1}$) consistent with Volmer-limited HER (hydrogen adsorption at the electrocatalyst surface). Spin-selective transport through the chiral catalyst **MeLTA-C**, which can induce spin alignment in oxidised radicals,[68] may explain the faster transport kinetics of **MeLTA-C** versus **MeTA-rac**. Although the CISS effect in HER is reported for photoelectrochemical water splitting,[45] wherein hydrogen evolution is promoted by spin filtering over chiral polymers, to our knowledge it has not been previously observed in electrocatalytic HER. Potentiodynamic stability of **MeLTA-C** was again evaluated through accelerated degradation (AD) experiments over 1000 cycles at a scan rate of 500 $mV.sec^{-1}$, and again only resulted in a small increase in overpotential (from 143 mV to

164 mV) after electrocatalysis in these acidic conditions (**Figure S18a**). This excellent electrochemical stability for HER was confirmed by chronoamperometry performed at -0.2 V versus RHE for 24 h (**Figure S18b**), which evidenced minimal decrease in current density. EIS measurements (**Figure 5c**) showed a lower R_{ct} across the electrode-electrolyte interface for **MeLTA-C** (4.0 Ω) than **MeTA-rac** (15.8 Ω), consistent with faster charge and mass transport for the chiral organoelectrocatalyst. Unpaired electrons at the catalyst surface can influence the adsorption strength of radical intermediates produced during electrocatalytic water splitting, which may further influence charge transfer across the electrode-electrolyte interface.[69]

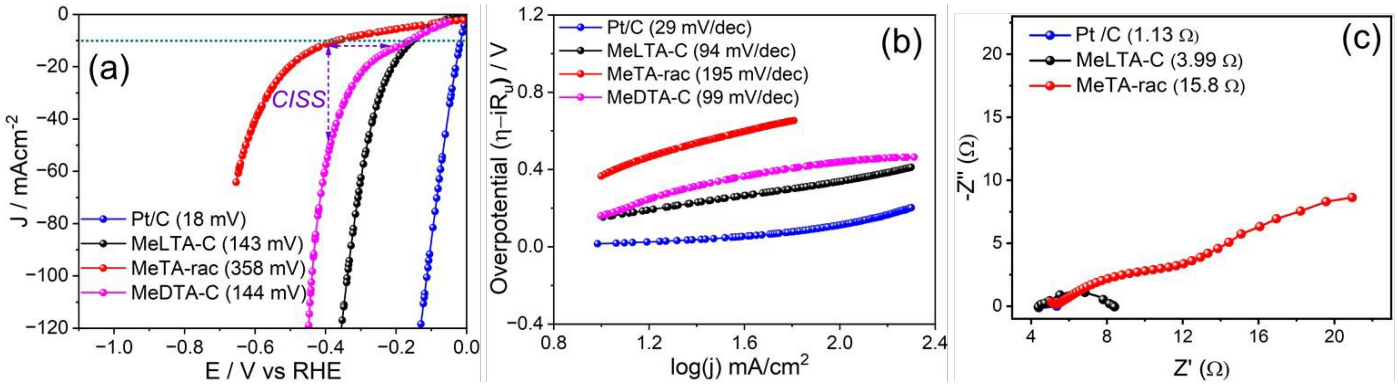

Figure 5. (a) LSV plots of **MeLTA-C, MeDTA-C** and **MeTA-rac** alongside a Pt/C reference for HER in 0.5 M H_2SO_4 under nitrogen, and corresponding (b) Tafel and (c) Nyquist plots, providing insight on HER kinetics and electron transfer dynamics at the electrode-electrolyte interface, respectively.

Alkaline HER is important for hydrogen production from alkaline wastewater discharged from chloralkali process (producing Cl_2 and NaOH) and other chemical industries.[70] Only a few, mostly defect-rich, heteroatom doped, organoelectrocatalysts, are reported for alkaline HER relative to the more popular acidic HER.[71, 72] The possibility of spin-selective transport over **MeLTA-C** was thus also investigated in alkaline HER using a 1 M KOH electrolyte. A lower overpotential was again observed for **MeLTA-C** (366 mV) and **MeDTA-C** (373 mV) as compared to **MeTA-rac** (511 mV), and more rapid increase in cathodic current with applied potential (**Figure 6a** and **S19a**). The higher overpotential for alkaline versus acidic HER reflects the stronger covalent H-O-H bond that must be cleaved to form H ad-atoms in the former scenario as previously reported.[70,73] At a common potential of -0.5 V vs RHE, the CISS effect resulted in a four-fold increase in current density for **MeLTA-C** with respect to **MeTA-rac**, approximately half the enhancement observed for acidic HER. Tafel plots similarly evidenced faster charge transfer (slope of 188 $mV.dec^{-1}$ versus 277 $mV.dec^{-1}$, **Figure S19b**) and a lower resistance to charge transfer across the electrode–electrolyte interface (R_{ct} of 5.13 Ω versus 7.47 Ω at constant overpotential, **Figure 6b**) for **MeLTA-C** than **MeTA-rac**. Note the overpotential for alkaline HER over **MeLTA-C** again compares favourably with literature reported organoelectrocatalysts (**Table S9**). Excellent electrocatalytic stability was also observed for **MeTA-rac** during alkaline HER, with the overpotential only 16 mV more negative (between 366 and 382 mV) after 1000 cycles at 150 $mV.sec^{-1}$ **(Figure S20**). Having demonstrated the effectiveness of **MeLTA-C** for electrocatalytic OER and HER under alkaline conditions, an electrochemical cell was assembled with **MeLTA-C** drop-cast on both anode and cathode for total water splitting under alkaline conditions; 10 $mA.cm^{-2}$ current density was achieved for a cell voltage of 1.98 V (**Figure S21**).

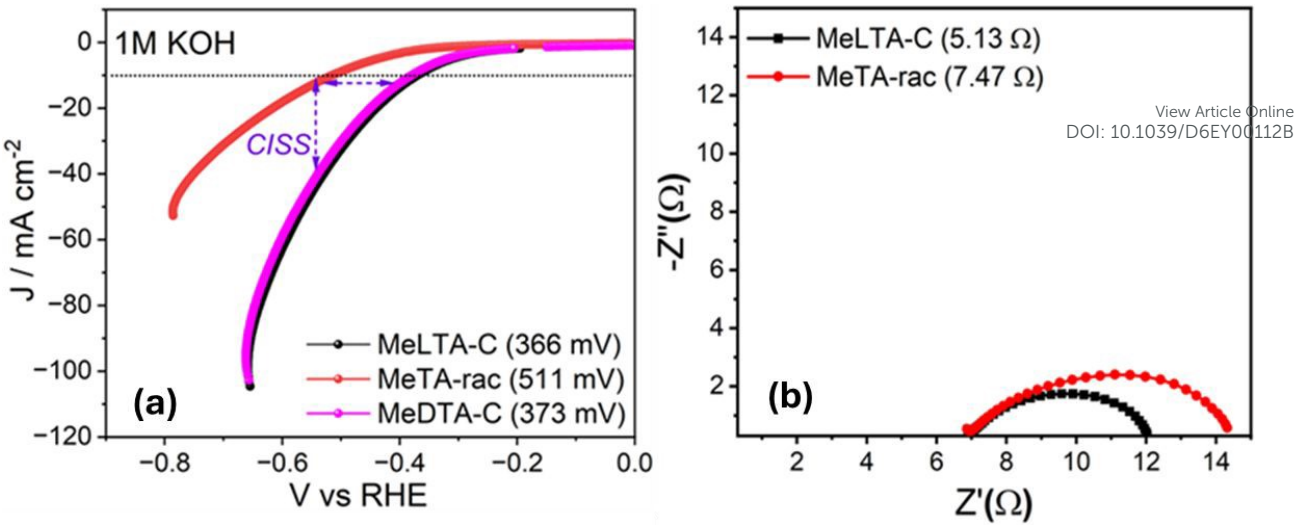

View Article Online
DOI: 10.1039/D6EY00112B

Figure 6. (a) LSV plots of **MeLTA-C** and **MeTA-rac** for HER in 1 M KOH under nitrogen, and (b) corresponding Nyquist plot demonstrating the lower interfacial charge transfer resistance of **MeLTA-C**.

The crystallinity and morphology of **MeLTA-C** recovered from the carbon cloth following alkaline OER and HER was also examined. Powder X-ray evidenced a significant loss of crystallinity compared to the as-synthesised **MeLTA-C** (**Figure S22-24a**), nevertheless reflections characteristic of the parent organoelectrocatalyst remained at ~16°, 18° and 27° (the latter a composite of multiple broadened reflections). FESEM also confirmed retention of the spiral arrangement of rectangular plates present in the parent **MeLTA-C** (**Figure S22-23b**). Together, these observations suggest that although **MeLTA-C** undergoes nanoscale restructuring during alkaline OER, its macroscopic properties are essentially unchanged. The chemical stability of **MeLTA-C** and **MeTA-rac** was further validated from the XPS, recorded for both materials after alkaline OER and HER (overall water splitting using the same catalyst at both electrodes). All expected elements were observed in the survey spectra, with corresponding high-resolution C, N, and O 1s XP spectra consistent with the expected atomic ratios and chemical environments (**Figure S25-26**).

In summary, the introduction of chirality (through L-(+)-tartaric acid/ D-(-)-tartaric acid) permits the synthesis of an inexpensive, crystalline and thermochemically stable organoelectrocatalyst (**MeLTA-C/ MeDTA-C**) that are more active[74] for alkaline OER and acidic and alkaline HER than their racemic counterpart. This manifests as a lower overpotential, and faster (interfacial) charge transfer for **MeLTA-C/MeDTA-C** versus an achiral analogue (**MeTA-rac**), and is attributed to a higher density of active sites, though we cannot discount the possibility that spin polarisation/filtering at the electrode-electrolyte interface also favours lower energy reactive intermediates and products (as proposed for chiral modified metal oxides in OER[16, 21, 31] and photo-electrocatalytic HER[45]). The hydrothermal synthesis of **MeLTA-C/ MeDTA-C** is amenable to scale-up (**Table S1**), and the methodology is adaptable to other chiral diacids (and/or chiral amines) to develop more active and energy-efficient organoelectrocatalysts for large-scale water splitting. Future work will explore the electronic conductivity, energetics, and photophysical properties of these organoelectrocatalysts and their purely ionic analogues to improve charge transport for commercial implementation.

4. Conclusions

Chiral-enhancement of water splitting over organoelectrocatalysts was explored for hydrogen-bonded, (ionised) melamine and tartaric acid co-crystals prepared by a facile hydrothermal synthesis in a racemic (**MeTA-rac**) or chiral (**MeLTA-C/ MeDTA-D**) form. The chiral organoelectrocatalysts exhibited a substantially reduced overpotential for

both the hydrogen evolution reaction (HER) and oxygen evolution reaction (OER) for current densities between 10-30 $mA.cm^{-2}$. For OER, the current density (activity) of **MeLTA-C/ MeDTA-C** was four times that of **MeTA-rac** at 1.68 V (attributed to a higher number of active sites), with a Faradaic efficiency of 90 % and good potentiodynamic stability. Similar enhancements were observed for HER under acidic and alkaline conditions, where Faradaic efficiencies reached 86 % and 85 %, respectively. Tafel slope analysis reveals faster charge transfer across the electrode-electrolyte interface and a change in the rate-limiting step, for **MeLTA-C/MeDTA-C** versus **MeTA-rac**, consistent with higher active site densities and/or spin-polarisation of radicals at the surface of the chiral catalyst selectively promoting HER and OER pathways. This enhancement also manifests in overall water splitting employing **MeLTA-C** electrocatalysts at both anode and cathode, i.e., an entirely organoelectrocatalytic system. Low cost and hydrothermally stable chiral organocatalysts offer new avenues for sustainable chemical manufacturing of renewable fuels and chemicals.

Notes

CCDC 2371296, 2516371 and CCDC 2370819 contain deposited data for **MeLTA-C, MeDTA-C**, and **MeTA-rac** respectively.

Author contributions

AC: methodology, data curation, formal analysis, validation, writing original draft (related to materials synthesis and characterization); AK: data curation, formal analysis, validation, writing original draft (related to electrocatalytic water splitting); HG: data curation (materials characterization); ST: crystallographic data curation and analysis; SM: supervision (AC); KW: fund acquisition, supervision (AC), writing – review & editing; AFL: fund acquisition, supervision (AC), writing – review & editing; SK: supervision (AK), writing – review & editing; JM: supervision (AC, HG), fund acquisition, writing – review & editing.

Acknowledgements

JM acknowledges funding from ANRF India (SERB-POWER Grant: SPG/2021/004430) and CSIR (CSIR FIRST: FIR030303). MEMED&CIF, CSIR-CSMCRI is acknowledged for instrumental facilities. KW and AFL acknowledge funding from the Australian Research Council Centre of Excellence - Green electrochemical transformation of CO2 (GETCO2, CE230100017). CSMCRI PRIS No. 55/2025

References:

1. Chu, S.; Majumdar, A. Opportunities and Challenges for a Sustainable Energy Future. *Nature* **2012**, *488*, 294–303. DOI: 10.1038/nature11475
2. Eisenberg, R.; Gray, H. B.; Crabtree, G. W. Addressing the Challenge of Carbon-Free Energy. *Proc. Natl. Acad. Sci. U.S.A.* **2020**, *117*, 12543–12549. DOI: 10.1073/pnas.1821674116
3. Roger, I.; Shipman, M. A.; Symes, M. D. Earth-Abundant Catalysts for Electrochemical and Photoelectrochemical Water Splitting. *Nat. Rev. Chem.* **2017**, *1*, 0003. DOI: 10.1038/s41570-016-0003
4. Lewis, N. S.; Nocera, D. G. Powering the Planet: Chemical Challenges in Solar Energy Utilization. *Proc. Natl. Acad. Sci. U.S.A.* **2006**, *103*, 15729–15735. DOI: 10.1073/pnas.0603395103

5. Seh, Z. W.; Kibsgaard, J.; Dickens, C. F.; Chorkendorff, I.; Nørskov, J. K.; Jaramillo, T. F. Combining Theory and Experiment in Electrocatalysis: Insights into Materials Design. *Science* **2017**, *355*, eaad4998. DOI: 10.1126/science.aad4998
View Article Online
DOI: 10.1039/D6EY00112B
6. Lee, C. H.; Jun, B.; Lee, S. U. Metal-Free Oxygen Evolution and Oxygen Reduction Reaction Bifunctional Electrocatalyst in Alkaline Media: From Mechanisms to Structure–Catalytic Activity Relationship. *ACS Sustainable Chem. Eng.* **2018**, *6*, 4973–4980. DOI: 10.1021/acssuschemeng.7b04608
7. Dau, H.; Limberg, C.; Reier, T.; Risch, M.; Roggan, S.; Strasser, P. The Mechanism of Water Oxidation: From Electrolysis via Homogeneous to Biological Catalysis. *ChemCatChem* **2010**, *2*, 724–761. DOI: 10.1002/cctc.201000126
8. Bockris, J. O. M. Kinetics of Activation Controlled Consecutive Electrochemical Reactions: Anodic Evolution of Oxygen. *J. Chem. Phys.* **1956**, *24*, 817–827. DOI: 10.1063/1.1742616
9. Che, M. Nobel Prize in Chemistry 1912 to Sabatier: Organic Chemistry or Catalysis? *Catal. Today* **2013**, *218–219*, 162–171. DOI: 10.1016/j.cattod.2013.07.006
10. Vesborg, P. C. K.; Seger, B.; Chorkendorff, I. Recent Development in Hydrogen Evolution Reaction Catalysts and Their Practical Implementation. *J. Phys. Chem. Lett.* **2015**, *6*, 951–957. DOI: 10.1021/acs.jpclett.5b00306
11. Park, S.; Shao, Y.; Liu, J.; Wang, Y. Oxygen Electrocatalysts for Water Electrolyzers and Reversible Fuel Cells: Status and Perspective. *Energy Environ. Sci.* **2012**, *5*, 9331–9344. DOI: 10.1039/C2EE22554A
12. Supanchaiyamat, N.; Hunt, A. J. Conservation of Critical Elements of the Periodic Table. *ChemSusChem* **2019**, *12*, 397–403. DOI: 10.1002/cssc.201802556
13. Franks, D. M.; Keenan, J.; Hailu, D. Mineral Security Essential to Achieving the Sustainable Development Goals. *Nat. Sustain.* **2023**, *6*, 21–27. DOI: 10.1038/s41893-022-00967-9
14. European Commission; Grohol, M.; Veeh, C. *Study on the Critical Raw Materials for the EU 2023*; Publications Office of the European Union: Luxembourg, 2023. https://data.europa.eu/doi/10.2873/725585
15. Garcés-Pineda, F. A.; Blasco-Ahicart, M.; Nieto-Castro, D.; López, N.; Galán-Mascarós, J. R. Direct Magnetic Enhancement of Electrocatalytic Water Oxidation in Alkaline Media. *Nat. Energy* **2019**, *4*, 519–525. DOI: 10.1038/s41560-019-0404-4
16. Vadakkayil, A.; Clever, C.; Kunzler, K. N.; Tan, S.; Bloom, B. P.; Waldeck, D. H. Chiral Electrocatalysts Eclipse Water Splitting Metrics through Spin Control. *Nat. Commun.* **2023**, *14*, 1067. DOI: 10.1038/s41467-023-36703-w
17. Mtangi, W.; Tassinari, F.; Vankayala, K.; Jentzsch, A. V.; Adelizzi, B.; Palmans, A. R. A.; Fontanesi, C.; Meijer, E. W.; Naaman, R. Control of Electrons' Spin Eliminates Hydrogen Peroxide Formation during Water Splitting. *J. Am. Chem. Soc.* **2017**, *139*, 2794–2798. DOI: 10.1021/jacs.6b12971
18. Fransson, J.; Turin, L. Current-Induced Spin Polarization in Chiral Molecules. *J. Phys. Chem. Lett.* **2024**, *15*, 6370–6374. DOI: 10.1021/acs.jpclett.4c01362
19. Naaman, R.; Paltiel, Y.; Waldeck, D. H. Chiral Induced Spin Selectivity Gives a New Twist on Spin-Control in Chemistry. *Acc. Chem. Res.* **2020**, *53*, 2659–2667. DOI: 10.1021/acs.accounts.0c00485
20. Chae, K.; Mohamad, N. A. R. C.; Kim, J.; Won, D.-I.; Lin, Z.; Kim, J.; Kim, D. H. The Promise of Chiral Electrocatalysis for Efficient and Sustainable Energy Conversion and Storage: A comprehensive review of the CISS effect and future directions . *Chem. Soc. Rev.* **2024**, *53*, 9029–9058. DOI: 10.1039/D3CS00316G
21. Kiran, V.; Mathew, S. P.; Cohen, S. R.; Delgado, I. H.; Lacour, J.; Naaman, R. Helicenes—A New Class of Organic Spin Filter. *Adv. Mater.* **2016**, *28*, 1957–1962. DOI: 10.1002/adma.201504725

22. Evers, F.; Aharony, A.; Bar-Gill, N.; Entin-Wohlman, O.; Hedegard, P.; Hod, O.; Jelinek, P.; Kamieniarz, G.; Lemeshko, M.; Michaeli, K.; Mujica, V.; Naaman, R.; Paltiel, Y.; Refaely-Abramson, S.; Tal, O.; Thijssen, J.; Thoss, M.; van Ruitenbeek, J. M.; Venkataraman, L.; Waldeck, D. H.; Yan, B.; Kronik, L. Theory of Chirality Induced Spin Selectivity: Progress and Challenges. *Adv. Mater.* **2022**, *34*, e2106629. DOI 10.1002/adma.202106629
23. Gupta, R.; Balo, A.; Garg, R.; Mondal, A. K.; Ghosh, K. B.; Mondal, P. C. The Chirality-Induced Spin Selectivity Effect in Asymmetric Spin Transport: From Solution to Device Applications. *Chem. Sci.* **2024**, *15*, 18751–18771. DOI: 10.1039/D4SC05736H
24. Chiesa, A.; Privitera, A.; Garlatti, E.; Allodi, G.; Bittl, R.; Wasielewski, M. R.; Sessoli, R.; Carretta, S. Chirality-Induced Spin Selectivity at the Molecular Level: A Different Perspective to Understand and Exploit the Phenomenon. *J. Phys. Chem. Lett.* **2025**, *16*, 5358–5372. DOI: 10.1021/acs.jpclett.5c00755
25. Bloom, B. P.; Paltiel, Y.; Naaman, R.; Waldeck, D. H. The Chirality-Induced Spin Selectivity Effect in Asymmetric Spin Transport: From Solution to Device Applications. *Chem. Rev.* **2024**, *124*, 1950–1991. DOI: 10.1021/acs.chemrev.3c00661
26. Mondal, P. C.; Kantor-Uriel, N.; Mathew, S. P.; Tassinari, F.; Fontanesi, C.; Naaman, R. Chiral Conductive Polymers as Spin Filters. *Adv. Mater.* **2015**, *27*, 1924–1927. DOI: 10.1002/adma.201405249
27. Wang, Z.; Wan, J.; Sun, X.; Sun, L.; Chen, S.; Zhang, Q. Boosting the Selectivity in Oxygen Electrocatalysis Using Chiral Nanoparticles as Electron-Spin Filters. *J. Am. Chem. Soc.* **2025**, *147*, 15767–15776. DOI: 10.1021/jacs.5c03394
28. Bhowmick, D. K.; Yuran, N.; Fadeev, M.; Yochelis, S.; Paltiel, Y.; Naaman, R. Chiral Metal Coating to Enhance Water Electrolysis. *Energy Fuels* **2025**, *39*, 764–770. DOI: 10.1021/acs.energyfuels.4c04304
29. Liang, Y.; Banjac, K.; Martin, K.; Zigon, N.; Lee, S.; Vanthuyne, N.; Garces-Pineda, F. A.; Galan-Mascaros, J. R.; Hu, X.; Avarvari, N.; Lingenfelder, M. Enhancement of Electrocatalytic Oxygen Evolution by Chiral Molecular Functionalization of Hybrid 2D Electrodes. *Nat. Commun.* **2022**, *13*, 3356. DOI: 10.1038/s41467-022-31096-8
30. Vadakkayil, A.; Dunlap-Shohl, W. A.; Joy, M.; Bloom, B. P.; Waldeck, D. H. Improved Catalyst Performance for the Oxygen Evolution Reaction under a Chiral Bias. *ACS Catal.* **2024**, *14*, 17303–17309. DOI: 10.1021/acscatal.4c04477
31. Zhang, W.; Banerjee-Ghosh, K.; Tassinari, F.; Naaman, R. Enhanced Electrochemical Water Splitting with Chiral Molecule-Coated Fe_3O_4 Nanoparticles. *ACS Energy Lett.* **2018**, *3*, 2308–2313. DOI: 10.1021/acsenergylett.8b01454
32. Bian, Z.; Kato, K.; Ogoshi, T.; Cui, Z.; Sa, B.; Tsutsui, Y.; Seki, S.; Suda, M. Hybrid Chiral MoS_2 Layers for Spin-Polarized Charge Transport and Spin-Dependent Electrocatalytic Applications. *Adv. Sci.* **2022**, *9*, e2201063. DOI: 10.1002/advs.202201063
33. Feng, T.; Chen, W.; Xue, J.; Cao, F.; Chen, Z.; Ye, J.; Xiao, C. Spin Polarization of Chiral Amorphous Fe–Ni Electrocatalysts Enabling Efficient Electrochemical Oxygen Evolution. *Adv. Funct. Mater.* **2023**, *33*, 2215051. DOI: 10.1002/adfm.202215051
34. Im, H.; Ma, S.; Lee, H.; Park, J.; Park, Y. S.; Yun, J.; Lee, J.; Moon, S.; Moon, J. Elucidating the Chirality Transfer Mechanisms during Enantioselective Synthesis for the Spin-Controlled Oxygen Evolution Reaction. *Energy Environ. Sci.* **2023**, *16*, 1187–1199. DOI: 10.1039/D2EE03853F

35. Grimm, O. C.; Somaratne, R.; Wang, Y.; Kim, S.; Whitten, J. E. Thiol Adsorption on Metal Oxide Nanoparticles. *Phys. Chem. Chem. Phys.* **2021**, *23*, 8309–8317. DOI: 10.1039/D1CP00506E

36. Yue, X.; Huang, S.; Cai, J.; Jin, Y.; Shen, P. K. Heteroatom Dual-Doped Porous Graphene Nanosheets as Efficient Bifunctional Metal-Free Electrocatalysts for Overall Water Splitting. *J. Mater. Chem. A* **2017**, *5*, 7784–7790. DOI: 10.1039/d3ma00859b

37. Zhao, Y.; Nakamura, R.; Kamiya, K.; Nakanishi, S.; Hashimoto, K. Nitrogen-Doped Carbon Nanomaterials as Non-Metal Electrocatalysts for Water Oxidation. *Nat. Commun.* **2013**, *4*, 2390. DOI: 10.1038/ncomms3390

38. Karak, S.; Koner, K.; Karmakar, A.; Mohata, S.; Nishiyama, Y.; Duong, N. T.; Thomas, N.; Ajithkumar, T. G.; Hossain, M. S.; Bandopadhyay, S.; Kundu, S.; Banerjee, R. Morphology Tuning via Linker Modulation: Metal-Free Covalent Organic Nanostructures with Exceptional Chemical Stability for Electrocatalytic Water Splitting. *Adv. Mater.* **2024**, *36*, e2209919. DOI: 10.1002/adma.202209919

39. Das, G.; Singha Roy, S.; Ibrahim, F. A.; Merhi, A.; Dirawi, H. N.; Benyettou, F.; Das, A. K.; Prakasam, T.; Varghese, S.; Sharma, S. K.; Kirmizialtin, S.; Jagannathan, R.; Gandara, F.; Aouad, S.; Olson, M. A.; Kundu, S.; Kaafarani, B. R.; Trabolsi, A. Electrocatalytic Water Splitting in Isoindigo-Based Covalent Organic Frameworks. *Angew. Chem. Int. Ed.* **2025**, *64*, e202419836. DOI: 10.1002/anie.202419836

40. Feng, J.-D.; Zhang, W.-D.; Gu, Z.-G. Covalent Organic Frameworks for Electrocatalysis: Design, Applications, and Perspectives. *ChemPlusChem* **2024**, *89*, e202400069. DOI: 10.1002/cplu.202400069

41. Basak, A.; Karmakar, A.; Dutta, S.; Roy, D.; Paul, S.; Nishiyama, Y.; Pathak, B.; Kundu, S.; Banerjee, R. Metal-Free Electrocatalytic Alkaline Water Splitting by Porous Macrocyclic Proton Sponges. *Angew. Chem. Int. Ed.* **2025**, *64*, e202419377. DOI: 10.1002/anie.202419377

42. Jena, H. S.; Krishnaraj, C.; Parwaiz, S.; Lecoeuvre, F.; Schmidt, J.; Pradhan, D.; Van Der Voort, P. Role of Quaternary-N of BINOL Covalent Triazine-Based Frameworks in Oxygen Reduction and Hydrogen Evolution Reactions. *ACS Appl. Mater. Interfaces* **2020**, *12*, 44689–44699. DOI: 10.1021/acsami.0c11381

43. Mirzakulova, E.; Khatmullin, R.; Walpita, J.; Corrigan, T.; Vargas-Barbosa, N. M.; Vyas, S.; Oottikkal, S.; Manzer, S. F.; Hadad, C. M.; Glusac, K. D. Electrode-Assisted Catalytic Water Oxidation by a Flavin Derivative. *Nat. Chem.* **2012**, *4*, 794–801. DOI: 10.1038/nchem.1439

44. Chhetri, A.; Karthick, K.; Karmakar, A.; Kundu, S.; Mitra, J. Melamine-Based Hydrogen-Bonded Systems as Organoelectrocatalysts for Water Oxidation Reaction. *ChemSusChem* **2023**, *16*, e202300220. DOI: 10.1002/cssc.202300220

45. Tassinari, F.; Banerjee-Ghosh, K.; Parenti, F.; Kiran, V.; Mucci, A.; Naaman, R. Enhanced Hydrogen Production with Chiral Conductive Polymer-Based Electrodes. *J. Phys. Chem. C* **2017**, *121*, 15777–15783. DOI: 10.1021/acs.jpcc.7b04194

46. Lemmerer, A.; Govindraju, S.; Johnston, M.; Motloung, X.; Savig, K. L. Co-Crystals and Molecular Salts of Carboxylic Acid/Pyridine Complexes. *CrystEngComm* **2015**, *17*, 3591–3595. DOI: 10.1039/C5CE00102A

47. Chand, S.; Deng, W.-H.; Pal, S. C.; Saha, A.; Manna, A. K.; Das, M. C. Biomimetic Water-Stable Multicomponent HOFs as Ultrahigh Superprotonic Conductors. *ACS Energy Lett*. **2025**, DOI: 10.1021/acsenergylett.5c02852

48. Chhetri, A.; Ahmad, S.; Podder, S.; Tothadi, S.; Maniam, S.; Reddy, C. M.; Mitra, J. Correlating Nanomechanical Behavior and Adsorption Performance in a Serendipitously Assembled Two-Dimensional Hydrogen-Bonded Organic System. *Langmuir* **2025**, DOI: 10.1021/acs.langmuir.5c04711

49. Nicholson, J. W.; Brookman, P. J.; Lacy, O. M.; Wilson, A. D. FTIR Study of the Role of Tartaric Acid in Glass-Ionomer Dental Cements. *J. Dent. Res.* **1988**, *67*, 1451–1454. DOI: 10.1177/00220345880670120
50. Liu, J.; Wang, C.; Song, Y.; Zhang, S.; Zhang, Z.; He, L.; Du, M. Two-Dimensional Triazine-Based Porous Framework as a Novel Metal-Free Bifunctional Electrocatalyst for Zinc–Air Battery. *J. Colloid Interface Sci.* **2021**, *591*, 253–263. DOI: 10.1016/j.jcis.2021.02.007
51. Brinkmann, A.; Litvinov, V. M.; Kentgens, A. P. Environmentally Friendly Flame Retardants: A Solid-State NMR Study of Melamine Orthophosphate. *Magn. Reson. Chem.* **2007**, *45*, S231–S246. DOI: 10.1002/mrc.2159
52. Johnson, J.; Saha, E.; Chhetri, A.; Suresh, E.; Mitra, J. Self-Assembled Melaminium Adipate Lamellae for Adsorptive Removal of Anionic Dyes. *ACS Appl. Polym. Mater.* **2021**, *3*, 651–660. DOI: 10.1021/acsapm.0c00955
53. Stevens, J. S.; Byard, S. J.; Seaton, C. C.; Sadiq, G.; Davey, R. J.; Schroeder, S. L. M. Proton Transfer and Hydrogen Bonding in the Organic Solid State. *Phys. Chem. Chem. Phys.* **2014**, *16*, 1150–1160. DOI: 10.1039/C3CP53907E
54. Chow, H.-F.; Mak, C. C. Preparation and Structure–Chiroptical Relationships of Tartaric Acid-Based Layer-Block Chiral Dendrimers. *J. Chem. Soc., Perkin Trans. 1* **1997**, 91–96. DOI: 10.1039/A604539A
55. Haghdani, S., Hoff, B. H., Koch, H. & Åstrand, P.-O. Solvent Effects on Optical Rotation: On the Balance between Hydrogen Bonding and Shifts in Dihedral Angles. *J. Phys. Chem. A* 2017, 121, 4765-4777. https://doi.org:10.1021/acs.jpca.6b12149
56. Zhou, B.; Zhao, Q.; Tang, L.; Yan, D. Tunable Room-Temperature Phosphorescence in Ratiometric Co-Crystals. *Chem. Commun.* **2020**, *56*, 7698–7701. DOI: 10.1039/D0CC02730H
57. Zhang, B.; Zhang, Y.; Hou, M.; Wang, W.; Hu, S.; Cen, W.; Cao, X.; Qiao, S.; Han, B.-H. Pristine and Metal Cluster Modified Conjugated Triazine Frameworks as Electrocatalysts for Hydrogen Evolution Reaction. *J. Mater. Chem. A* **2021**, *9*, 10146–10159. DOI: 10.1039/D1TA00589H
58. Karmakar, A.; Mahendiran, D.; Madhu, R.; Murugan, P.; Kundu, S. Bypassing the Scaling Relationship with Spin Selectivity : Construction of Lewis Base-Functionalized Heterostructural 2D Nanosheets for Enhanced Oxygen Evolution Reaction. *J. Mater. Chem. A* **2023**, *11*, 16349–16362. DOI: 10.1039/D3TA02815A
59. Wang, Q.; Ji, Y.; Lei, Y.; Wang, Y.; Wang, Y.; Li, Y.; Wang, S. Pyridinic-N-Dominated Defective Graphene as a Superior Oxygen Electrocatalyst for Ultrahigh-Energy-Density Zn-Air Batteries. *ACS Energy Lett.* **2018**, *3*, 1183–1191. DOI: 10.1021/acsenergylett.8b00303
60. Zhao, M.; Zhang, J.; Xiao, H.; Hu, T.; Jia, J.; Wu, H. Facile in situ Synthesis of a Carbon Quantum Dot/Graphene Heterostructure as an Efficient Metal-free Electrocatalyst for Overall Water Splitting. *Chem. Commun.* **2019**, *55*, 1635–1638. DOI: 10.1039/C8CC09368G
61. Aiyappa, H. B.; Thote, J.; Shinde, D. B.; Banerjee, R.; Kurungot, S. Cobalt-Modified Covalent Organic Framework as a Robust Water Oxidation Electrocatalyst. *Chem. Mater.* **2016**, *28*, 4375–4379. DOI: 10.1021/acs.chemmater.6b01370
62. Laouini, E.; Hamdani, M.; Pereira, M. I. S.; Douch, J.; Mendonca, M. H.; Berghoute, Y.; Singh, R. N. Preparation and Electrochemical Characterization of Spinel-Type Fe–Co_3O_4 Thin Film Electrodes in Alkaline Medium. *Int. J. Hydrogen Energy* **2008**, *33*, 4936–4944. DOI: 10.1016/j.ijhydene.2008.07.039
63. Wu, T.; Xu, Z. J. Oxygen Evolution in Spin-Sensitive Pathways. *Curr. Opin. Electrochem.* **2021**, *30*, 100804. DOI: 10.1016/j.coelec.2021.100804

64. Wu, T.; Ren, X.; Sun, Y.; Sun, S.; Xian, G.; Scherer, G. G.; Fisher, A. C.; Mandler, D.; Ager, J. W.; Grimaud, A.; Wang, J.; Shen, C.; Yang, H.; Gracia, J.; Gao, H.-J.; Xu, Z. J. Spin Pinning Effect to Reconstructed Oxyhydroxide Layer on Ferromagnetic Oxides for Enhanced Water Oxidation. *Nat. Commun.* **2021**, *12*, 3634. DOI: 10.1038/s41467-021-23896-1

65. Dette, C.; Hurst, M. R.; Deng, J.; Nellist, M. R.; Boettcher, S. W. Structural Evolution of Metal (Oxy)hydroxide Nanosheets during OER. *ACS Appl. Mater. Interfaces* **2019**, *11*, 5590–5594. DOI: 10.1021/acsami.8b02796
66. Patra, B. C.; Khilari, S.; Manna, R. N.; Mondal, S.; Pradhan, D.; Pradhan, A.; Bhaumik, A. A Metal-Free Covalent Organic Polymer for Electrocatalytic Hydrogen Evolution. *ACS Catal.* **2017**, *7*, 6120–6127. DOI: 10.1021/acscatal.7b01067
67. Bhunia, S.; Das, S. K.; Jana, R.; Peter, S. C.; Bhattacharya, S.; Addicoat, M.; Bhaumik, A.; Pradhan, A. Electrochemical Stimuli-Driven Facile Metal-Free Hydrogen Evolution from Pyrene-Porphyrin-Based Crystalline Covalent Organic Framework. *ACS Appl. Mater. Interfaces* **2017**, *9*, 23843–23851. DOI: 10.1021/acsami.7b06968
68. Naaman, R.; Waldeck, D. H. Spintronics and Chirality: Spin Selectivity in Electron Transport. *Annu. Rev. Phys. Chem.* **2015**, *66*, 263–281. DOI: 10.1146/annurev-physchem-040214-121554
69. Gracia, J. Itinerant Spins and Bond Lengths in Oxide Electrocatalysts for Oxygen Evolution and Reduction Reactions. *J. Phys. Chem. C* **2019**, *123*, 9967–9972. DOI: 10.1021/acs.jpcc.9b01635
70. Mahmood, N.; Yao, Y.; Zhang, J.-W.; Pan, L.; Zhang, X.; Zou, J.-J. Electrocatalysts for Hydrogen Evolution in Alkaline Electrolytes Mechanisms, Challenges, and Prospective Solutions. *Adv. Sci.* **2018**, *5*, 1700464. DOI: 10.1002/advs.201700464
71. Zhang, J.; Dai, L. Nitrogen, Phosphorus and Fluorine Tri-Doped Graphene as a Multifunctional Catalyst for Self-Powered Water Splitting. *Angew. Chem. Int. Ed.* **2016**, *55*, 13296–13300. DOI: 10.1002/anie.201607405
72. Jia, Y.; Zhang, L.; Du, A.; Gao, G.; Chen, J.; Yan, X.; Brown, C. L.; Yao, X. Defect Graphene as a Trifunctional Catalyst for Electrochemical Reactions. *Adv. Mater.* **2016**, *28*, 9532–9538. DOI: 10.1002/adma.201602912
73. Hu, H.; Qiao, M.; Pei, Y.; Fan, K.; Li, H.; Zong, B.; Zhang, X. Kinetics of Hydrogen Evolution in Alkali Leaching of Ni–Al Alloy. *Appl. Catal. A* **2003**, *252*, 173–183. DOI: 10.1016/S0926-860X(03)00416-2
74. Naaman, R.; Paltiel, Y.; Waldeck, D. H. Chiral Molecules and the Spin Selectivity Effect. *J. Phys. Chem. Lett.* **2020**, *11*, 3660–3666. DOI: 10.1021/acs.jpclett.0c00474

View Article Online
DOI: 10.1039/D6EY00112B

Data availability

The data supporting this article have been included as part of the Supplementary Information.

Crystallographic data for **MeLTA-C, MeDTA-C**, and **MeTA-rac** has been deposited at the Cambridge Crystallographic Database Centre (CCDC) under CCDC 2371296, 2516371 and CCDC 2370819 respectively.